Mon. Not. R. Astron. Soc. **372,** 591–608 (2006) doi:10.1111/j.1365-2966.2006.10886.x

The *XMM* Large-Scale Structure survey: a well-controlled X-ray cluster sample over the D1 CFHTLS area*

M. Pierre,[1]† F. Pacaud,[1] P.-A. Duc,[1] J. P. Willis,[2] S. Andreon,[3] I. Valtchanov,[4]‡ B. Altieri,[5] G. Galaz,[6] A. Gueguen,[1] J.-P. Le Fèvre,[7] O. Le Fèvre,[8] T. Ponman,[9] P.-G. Sprimont,[10] J. Surdej,[10] C. Adami,[8] A. Alshino,[9] M. Bremer,[11] L. Chiappetti,[12] A. Detal,[10] O. Garcet,[10] E. Gosset,[10] C. Jean,[10] D. Maccagni,[12] C. Marinoni,[8] A. Mazure,[8] H. Quintana[6] and A. Read[13]

[1] *DAPNIA/SAp CEA Saclay, 91191 Gif sur Yvette*
[2] *Department of Physics and Astronomy, University of Victoria, Elliot Building, 3800 Finnerty Road, Victoria, BC, Canada V8P 1A1*
[3] *INAF – Osservatorio Astronomico di Brera, Milan, Italy*
[4] *Astrophysics Group, Blackett Laboratory, Imperial College of Science Technology and Medicine, London SW7 2BW*
[5] *ESA, Villafranca del Castillo, Spain*
[6] *Departamento de Astronomía y Astrofísica, Pontificia Universidad Católica de Chile, Santiago, Chile*
[7] *DAPNIA/SEDI CEA Saclay, 91191 Gif sur Yvette*
[8] *Laboratoire d'Astrophysique de Marseille, France*
[9] *School of Physics and Astronomy, University of Birmingham, Edgebaston, Birmingham B15 2TT*
[10] *Université de Liège, Allée du 6 Août, 17, B5C, 4000 Sart Tilman, Liège Belgium*
[11] *Department of Physics, University of Bristol, Tyndall Avenue, Bristol BS8 1TL*
[12] *INAF – IASF Milan, Italy*
[13] *Department of Physics and Astronomy, University of Leicester, Leicester LE1 7RH*

Accepted 2006 July 25. Received 2006 July 25; in original form 2005 December 20

ABSTRACT

We present the *XMM* Large-Scale Structure Survey (*XMM*-LSS) cluster catalogue corresponding to the Canada–France–Hawaii Telescope Legacy Survey D1 area. The list contains 13 spectroscopically confirmed, X-ray selected galaxy clusters over 0.8 $\deg^2$ to a redshift of unity and so constitutes the highest density sample of clusters to date. Cluster X-ray bolometric luminosities range from 0.03 to 5×10^{44} erg s^{-1}. In this study, we describe our catalogue construction procedure: from the detection of X-ray cluster candidates to the compilation of a spectroscopically confirmed cluster sample with an explicit selection function. The procedure further provides basic X-ray products such as cluster temperature, flux and luminosity. We detected slightly more clusters with (0.5–2.0 keV) X-ray fluxes of $>2 \times 10^{-14}$ erg s^{-1} cm^{-2} than we expected based on expectations from deep *ROSAT* surveys. We also present the luminosity–temperature relation for our nine brightest objects possessing a reliable temperature determination. The slope is in good agreement with the local relation, yet compatible with a luminosity enhancement for the $0.15 < z < 0.35$ objects having $1 < T < 2$ keV, a population that the *XMM*-LSS is identifying systematically for the first time. The present study permits the compilation of cluster samples from *XMM* images whose selection biases are understood. This allows, in addition to studies of large-scale structure, the systematic investigation of cluster scaling law evolution, especially for low mass X-ray groups which constitute the bulk of our observed cluster population. All cluster ancillary data (images, profiles, spectra) are made available in electronic form via the *XMM*-LSS cluster data base.

Key words: surveys – X-rays: galaxies: clusters.

1 INTRODUCTION

The question of cosmic structure formation is substantially more complicated than the study of the spherical collapse of a pure dark matter perturbation in an expanding universe. While it is possible to predict theoretically how the shape of the inflationary

---

*Based on data collected with *XMM*, VLT, Magellan, NTT and CFH telescopes; ESO programme numbers are 070.A-0283, 070.A-907 (VVDS), 072.A-0104, 072.A-0312, 074.A-0360 and 074.A-0476.

†E-mail: mpierre@cea.fr

‡Present address: ESA, Villafranca del Castillo, Spain.

fluctuation spectrum evolves until recombination, understanding the subsequent formation of galaxies, active galactic nucleus (AGN) and galaxy clusters is complicated by the physics of non-linear growth and feedback from star formation. Attempts to use the statistics of visible matter fluctuations to constrain the nature of dark matter and dark energy are therefore reliant upon an understanding of non-gravitational processes.

Clusters, as the most massive entities of the Universe, form a crucial link in the chain of understanding. They lie at the nodes of the cosmic network, possess virialized cores, yet are still growing by accretion along filaments. The rate at which clusters form, and the evolution of their space distribution, depends strongly on the shape and normalization of the initial power spectrum, as well as on the dark energy equation of state (e.g. Rapetti, Allen & Weller 2005). Consequently, both a three-dimensional map of the cluster distribution and an evolutionary model relating cluster observables to cluster masses and shapes (predicted by theory for the average cluster population) are needed to test the consistency of structure formation models within a standard cosmology with the properties of clusters in the low-z Universe.

The main goal of the *XMM* Large-Scale Structure Survey (*XMM*-LSS) is to provide a well-defined statistical sample of X-ray galaxy clusters to a redshift of unity over a single large area, suitable for cosmological studies (Pierre et al. 2004). In this paper, we present the first sample of *XMM*-LSS clusters for which canonical selection criteria are uniformly applied over the survey area. In this way, we demonstrate the properties of the survey along with a description of data analysis tools employed in the sample construction; the aim being to provide a deep and well-controlled sample of clusters and to investigate evolution trends, in particular for the low end of the cluster mass function. The paper will therefore act as a reference for future studies using *XMM*-LSS data. The chosen region is located at $36^\circ < \mathrm{RA} < 37^\circ$, $-5^\circ < \mathrm{Dec.} < -4^\circ$. This region is known as D1, one of the four deep areas of the Canada–France–Hawaii Telescope Legacy Survey[1] (CFHTLS). It also includes one of the VIMOS VLT Deep Survey patches (VVDS; Ilbert et al. 2005) and was observed at 1.4 GHz down to the μJy level by the VLA-VIRMOS Deep Field (Bondi et al. 2003). The rest of the *XMM*-LSS survey surrounds D1 and corresponds to part of the wide W1 CFHTLS component (see Pierre et al. 2004 for a general layout and associated multi-λ surveys) for which the complete cluster catalogue will be published separately. The sample is the result of a fine tuned X-ray plus optical approach developed with the aim of understanding the various selection effects. We describe the catalogue construction procedure in tandem with a companion paper presenting a detailed description of the X-ray pipeline developed as part of the *XMM*-LSS survey (Pacaud et al. 2006).

The deepest published statistical samples of X-ray clusters over a contiguous sky area to date are all based on the *ROSAT* All-Sky Survey (RASS): REFLEX (Böhringer et al. 2001), NORAS (Böhringer et al. 2000), NEP (Henry et al. 2001). In parallel, a number of serendipitous cluster surveys were conducted using deep *ROSAT* pointings with the goal of investigating the evolution of the cluster luminosity function, for example, Southern SHARC (Burke et al. 1997), RDCS (Rosati et al. 1998), 160 deg^2 (Vikhlinin et al. 1998), Bright SHARC (Romer et al. 2000), BMW (Moretti et al. 2004). The advent of the *XMM* satellite has provided an X-ray imaging capability of increased sensitivity and angular resolving power compared to *ROSAT*. The *XMM*-LSS employs 1–20 ks pointings and samples the cluster population to a depth of $\sim 10^{-14}\,\mathrm{erg\,s^{-1}\,cm^{-2}}$ – a flux sensitivity comparable to the deepest serendipitous *ROSAT* surveys (Rosati, Borgani & Norman 2002). However, *XMM* observations possess a narrower point spread function [PSF; full width at half-maximum (FWHM) ∼6 arcsec for *XMM* versus ∼20 arcsec for the *ROSAT* PSPC] which suggests that the reliable identification of extended sources can be performed for apparently smaller sources. Instrumental characteristics such as background noise and the complex focal plane configuration are also quite different. In this context, our dual aim of optimizing the *XMM*-LSS sensitivity and of quantifying the many selection biases led us to develop a dedicated source detection pipeline as well as specific optical identification and spectroscopic confirmation procedures: special attention is given to extended, X-ray faint sources whose identification requires deep optical/IR multicolour imaging. These steps are described in Section 2 along with the presentation of the D1 cluster catalogue. Section 3 presents the X-ray properties of the newly assembled sample and some optical characteristics. Section 4 summarizes the global properties of our sample within the context of a 'concordance' cosmological model. We conclude with a discussion of our cluster selection function in comparison with earlier works as well as the scaling laws for the low end of the cluster mass function.

Throughout the paper we assume $\Omega_\mathrm{M} = 0.27, \Omega_\Lambda = 0.73$ and $H_0 = 71\,\mathrm{km\,s^{-1}\,Mpc^{-1}}$. All X-ray flux measures are quoted in the [0.5–2] keV band. The generic name 'cluster' refers to the entire population of gravitationally bound galaxy systems, while we use the term 'groups' for those systems whose potential corresponds to an X-ray temperature lower than 2 keV.

2 THE X-RAY CLUSTER CATALOGUE

2.1 X-ray observations

The *XMM*-LSS D1 region consists of a mosaic of 10 *XMM* pointings that form part of the *XMM* Medium Deep Survey (XMDS; Chiappetti et al. 2005). The pointing layout is displayed in Fig. 1 and the properties of individual pointings are shown in Table 1. The nominal exposure per pointing is 20 ks for this subregion,[2] with the exception of pointing G07, whose nominal exposure time of 40 ks was reduced to ∼20 effective ks as a result of solar activity. The raw X-ray observations (ODFs) were reduced using the standard *XMM* Science Analysis System (XMMSAS version v6.1) tasks emchain and epchain for the MOS and PN detectors, respectively. High background periods, related to soft protons, were excluded from the event lists following the procedure outlined by Pratt & Arnaud (2002). Raw photon images in different energy bands were then created with a scale of $2.5\,\mathrm{arcsec\,pixel^{-1}}$. A complete discussion of the image analysis and source characterization procedures are provided by Pacaud et al. (2006). Cluster detection was performed in the [0.5–2] keV band and was limited to the inner 11 arcmin of the *XMM* field. The total scanned area is $0.81\,\mathrm{deg}^2$. Information regarding the individual pointings is summarized in Table 1 and the layout of the pointings on the sky displayed in Fig. 1.

---

[1] http://cdsweb.u-strasbg.fr:2001/Science/CFHLS/

[2] Outside the XMDS, the nominal exposure per pointing for the rest of the *XMM*-LSS is 10 ks.

Table 1. Properties of individual *XMM* pointings. Quoted exposures are effective exposures computed after filtering high background periods.

Internal ID	*XMM* ID	RA (J2000)	Dec. (J2000)	MOS1, MOS2, pn exposure times (ks)
G01	0112680201	02:27:20.0	−04:10:00.0	24.6, 25.3, 21.4
G02	0112680201	02:26:00.0	−04:10:00.0	10.1, 9.7, 6.7
G03	0112680301	02:24:40.0	−04:10:00.0	21.8, 21.7, 17.3
G05	0112680401	02:28:00.0	−04:30:00.0	23.5, 23.9, 12.5
G06	0112681301	02:26:40.0	−04:30:00.0	16.4, 16.6, 10.5
G07	0112681001	02:25:20.0	−04:30:00.0	22.5, 25.1, 18.6
G08	0112680501	02:24:00.0	−04:30:00.0	21.2, 21.3, 15.9
G10	0109520201	02:27:20.0	−04:50:00.0	24.7, 24.6, 18.5
G11	0109520301	02:26:00.0	−04:50:00.0	21.7, 21.8, 16.1
G12	0109520401	02:24:40.0	−04:50:00.0	Not usable because of very high flare rate

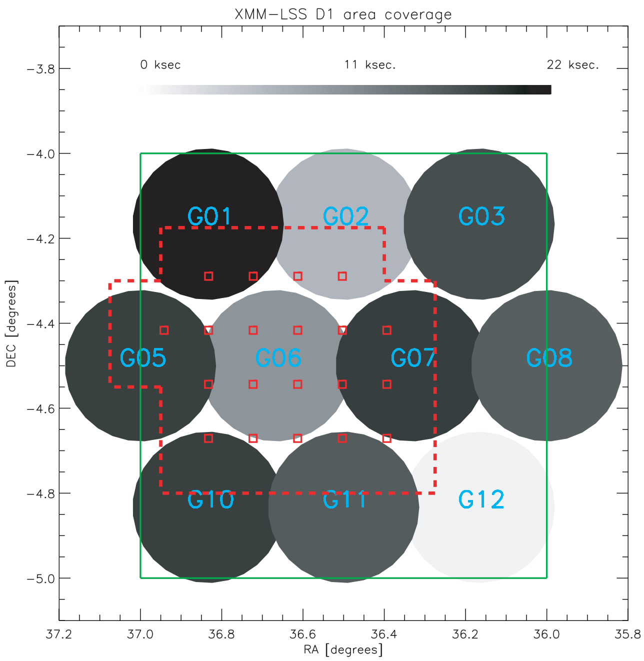

Figure 1. The *XMM* pointing mosaic over the D1 area (green square). The radius of the displayed pointings is 11 arcmin. The grey-scale indicates effective mean exposure time per detector, after removal of high background periods. The red squares show the centres of the VVDS pointings (Ilbert et al. 2005) and the red dotted line indicates the total area covered by the VVDS. The VLA-VIRMOS Deep Field encompasses exactly the D1 region.

2.2 Cluster X-ray detection and optical identification procedure

The compilation of an X-ray cluster sample featuring positional and redshift data ultimately requires the input of optical and/or near-infrared (NIR) data in order to select putative cluster galaxies for which precise redshifts can be obtained. Therefore, although X-ray selection is employed to better avoid projection effects, to provide direct clues about cluster masses and to provide more easily tractable selection criteria, optical/NIR data for each cluster must be assessed in order to obtain cluster redshift data. The goal of *XMM*-LSS is to produce a faint, statistical cluster catalogue over a wide spatial area (several tens of square degrees) and a large redshift interval (zero to unity). Cluster identification procedures must therefore identify robustly a wide range of cluster properties at both X-ray and optical/NIR wavelengths. Given the above requirements the *XMM*-LSS has developed over the last three years from initially simple and very robust cluster selection procedures to a refined, quantitative approach focusing on key cluster selection parameters.

Developing the X-ray pipeline was an essential part of the procedure as is reflected in the successive publications. We summarize these developments below.

(i) Spectroscopic observations during 2002 were performed for a number of cluster candidates identified following the method developed by (Valtchanov, Pierre & Gastaud 2001); extended X-ray sources were accepted as candidate clusters if associated with a spatial overdensity of galaxies displaying a uniform red colour sequence determined using either CFHT/CFH12K *BVRI* or CTIO/MOSAIC *Rz* imaging. This approach maximized the success rate of the first *XMM*-LSS spectroscopic observations (conducted in the last quarter of 2002) which demonstrated that clusters to a redshift of 1 are detectable with 1–20 ks *XMM* observations (Valtchanov et al. 2004; Willis et al. 2005).

(ii) In order to proceed towards a purely X-ray selected sample – that is, to reduce contamination by spurious extended sources – a maximum likelihood procedure named XAMIN was combined with the wavelet-based detection algorithm developed previously (Pierre et al. 2004). The sample of candidate clusters thus generated was investigated during the spectroscopic observations conducted in 2003 and 2004.

(iii) Finally, the combination of spectroscopic results for the above cluster sample with a detailed study of the simulated performance of the X-ray pipeline led to the definition of three clearly defined classes of X-ray cluster candidates.

The cluster identification procedure described above satisfies the goal of generating a relatively uncontaminated sample of X-ray clusters with a well-defined selection function. A detailed description of the X-ray parameters employed to generate each class of cluster candidate is described in the following section.

2.3 The cluster classification and sample

The ability to detect faint, extended sources in X-ray images is subject to a number of factors. Although the apparent size of a typical cluster ($R_c = 180$ kpc) is significantly larger than the *XMM* PSF (on-axis FWHM ∼6 arcsec) at any redshift of interest,[3] it is incorrect to assume that all clusters brighter than a given flux will be detected – unless the flux limit is set to some high value. Cluster

---

[3] $100 > R_c > 20$ arcsec for $0.1 < z < 1$.

detectability depends not only on the instrumental PSF, object flux and morphology but also upon the background level and the detector topology (e.g. CCD gaps and vignetting), in addition to the ability of the pipeline to separate close pairs of point-like sources – all of which are a function of the specified energy range (Scharf 2002). We thus stress that the concept of 'sky coverage', that is, the fraction of the survey area covered at a given flux limit, is strictly valid only for point sources because, for faint extended objects, the detection efficiency is surface brightness limited (rather than flux limited). Moreover, since the faint end of the cluster luminosity function is poorly characterized at $z > 0$, it is not possible to estimate a posteriori what fraction of groups remain undetected, unless a cosmological model is assumed, along with a thorough modelling of the cluster population out to high redshift; the lower limit of the mass or luminosity function being here a key ingredient. To our knowledge, this has never been performed in a fully self-consistent way so far for any deep X-ray cluster survey ($F_{\rm lim} \sim 2$–$5 \times 10^{-14}\,{\rm erg\,s^{-1}\,cm^{-2}}$). It is also important to consider that the flux recorded from a particular cluster represents only some fraction of the total emitted flux and must therefore be corrected by integrating an assumed spatial emission model to large radius.

Consequently, with the goal of constructing deep controlled samples suitable for cosmology we define, rather than flux limits, classes of extended sources. These are defined in the extension and significance parameter space and correspond to specific levels of contamination and completeness. As shown by Pacaud et al. (2006), extensive simulations of various cluster and AGN populations generate detection probabilities as a function of sources properties. This enables a simultaneous estimate of the source completeness levels and of the frequency of contamination by misclassified point-like sources or spurious detections. X-ray source classification was performed using XAMIN and employs the output parameters: extent, likelihood of extent, likelihood of detection. The reliability of the adopted selection criteria has been checked against the current sample of 60 spectroscopically confirmed *XMM*-LSS clusters. We have defined three classes of extended sources as follows.

(i) The C1 class is defined such that no point sources are misclassified as extended and is described by extent > 5 arcsec, likelihood of extent >33 and likelihood of detection >32. The C1 class contains the highest surface brightness extended sources and inevitably includes a few nearby galaxies – these are readily discarded from the sample by inspection of optical overlays.

(ii) The C2 class is described by extent >5 arcsec and 15 < likelihood of extent <33 and typically displays a contamination rate of 50 per cent. The C2 class includes clusters fainter than C1, in addition to a number of nearby galaxies. Contaminating sources include saturated point sources, unresolved pairs, and sources strongly masked by CCD gaps, for which not enough photons were available to permit reliable source characterization. Contaminating sources were removed after a visual inspection of the optical/NIR data for each field and in some cases as a result of follow-up spectroscopy.

(iii) The C3 class was constructed in order to investigate clusters at the survey sensitivity limit, particularly clusters at high redshift. Sources within the C3 class typically display 2 < extent < 5 arcsec and likelihood of extent > 4. Selecting such faint, marginally extended sources generates a high contamination rate. However, low selection thresholds are required to identify extended sources at the survey limit: faint sources will never be characterized by high likelihood values. When refining the C3 class, the X-ray, optical and NIR appearance was examined thoroughly. Generally speaking, C3 sources display low surface brightness or extended emission affected by a point source. Additional constraints included that the detection should be located at an off-axis angle <10 arcmin and that the total detection should generate 30 photons or greater (stronger constraint on the off-axis value is necessary because weak objects are subject to strong distortions beyond 10 arcmin, thus hardly measurable). The most plausible C3 candidates were investigated spectroscopically and confirmed clusters are presented.

The analysis of simulated cluster and AGN data permits the computation of selection probabilities for the C1 and C2 cluster samples.[4] The extent to which the C1 and C2 classes are comparable to flux-limited samples is analysed in detail by Pacaud et al. (2006) and further discussed in the last section of this paper. The selection probability for C3 clusters has not been determined.

2.4 Determination of cluster redshifts

The *XMM*-LSS spectroscopic Core Programme aims at the redshift confirmation of the X-ray cluster candidates; velocity dispersion may subsequently be obtained for a subsample of confirmed clusters as a second step programme. Spectroscopic observations were performed using a number of telescope and instrument combinations and are summarized in Table 2. Details of which observing configuration was employed for each cluster are presented in Table 3.

The minimum criterion required to confirm a cluster was specified to be three concordant redshifts (±3000 km s^{-1}) within a projected scale of approximately 500 kpc of the X-ray emission centroid, computed at the putative cluster redshift. For nearby X-ray clusters of temperature $T_{\rm X} = 2$ keV, a radius of 500 kpc corresponds to approximately 50 per cent of the virial radius and encloses 66 per cent of the total mass – with both fractions being larger for higher temperature clusters (Arnaud, Pointecouteau & Pratt 2005). The final cluster redshift was computed from the non-weighted mean of all galaxies within this projected aperture and within a rest-frame velocity interval ±3000 km s^{-1} of the interactively determined redshift peak. Potential cluster galaxies are selected for spectroscopic observation by identifying galaxies displaying a uniformly red colour distribution within a spatial aperture centred on the extended X-ray source (see Andreon et al. 2005, for more details). Cluster members flagged via this procedure are then allocated spectroscopic slits in order of decreasing apparent magnitude (obviously avoiding slit overlap).

The exact observing conditions for each cluster form a heterogeneous distribution. However, each cluster was typically observed with a single spectroscopic mask featuring slitlets of 8–10 arcsec in length and 1–1.4 arcsec in width. The use of a different telescope and instrument configuration generally restricts the available candidate cluster member sample to a different limiting *R*-band magnitude (assuming an approximately standard exposure time of 2 h per spectroscopic mask). Typical apparent *R*-band magnitude limits generating spectra of moderate (S/N > 5) quality for each telescope were found to be the following: VLT/FORS2 (23), Magellan/LDSS2 (22) and NTT/EMMI (21.5). Spectroscopic data reduction followed standard IRAF[5] procedures. Redshift determination was performed by cross-correlating reduced, one-dimensional spectra with suitable

---

[4] The C1 and C2 classes are defined from simulations representative of a mean exposure time of 10 ks. In the present paper, we keep the same definition as the signal-to-noise ratio (S/N) increase is only $\sqrt{2}$.

[5] IRAF is distributed by the National Optical Astronomy Observatories, which are operated by the Association of Universities for Research in Astronomy, Inc., under cooperative agreement with the National Science Foundation.

Table 2. Observing resources employed to determine cluster spectroscopic redshifts.

Telescope	Instrument	Grism + filter	Approximate resolving power (*R*)	Identifier
VLT	FORS2	300V + GC435	500	1
VLT	FORS2	600RI + GC435	1000	2
VLT	FORS2	600z	1300	3
NTT	EMMI	Grism #3	700	4
Magellan (Clay)	LDSS-2	Medium red	500	5
VLT	VIMOS	LRRED	220	6

Table 3. Spectroscopically confirmed X-ray clusters within the D1 area.

Source	XLSSC	RA (°)	Dec. (°)	*XMM* pointings	Off-axis angle[a] (arcmin)	Redshift	# of members[b]	Observed (see Table 2)
C1								
XLSS J022404.1−041329[c]	029	36.0172	−4.2247	G03	9.0	1.05	5	3
XLSS J022433.5−041405	044	36.1410	−4.2376	G03	3.8	0.26	9	4
XLSS J022524.5−044042	025	36.3526	−4.6791	G07	10.3	0.26	10	5
XLSS J022530.6−041419	041	36.3777	−4.2388	G02	9.1	0.14	9	4
XLSS J022609.7−045804	011	36.5403	−4.9684	G11	8.1	0.05	7	4
XLSS J022709.1−041759[d]	005	36.7877	−4.3002	G01	7.8	1.05	5	2
XLSS J022725.8−043213[e]	013	36.8588	−4.5380	G05	8.1	0.31	11	5
XLSS J022739.9−045129	022	36.9178	−4.8586	G10	5.6	0.29	5	5
C2								
XLSS J022725.0−041123	038	36.8536	−4.1920	G01	1.9	0.58	7	4
C3								
XLSS J022522.7−042648	a	36.3454	−4.4468	G07	3.9	0.46	4	2
XLSS J022529.6−042547	b	36.3733	−4.4297	G07	5.8	0.92	7	6
XLSS J022609.9−043120	c	36.5421	−4.5226	G06	8.0	0.82	8	6
XLSS J022651.8−040956	d	36.7164	−4.1661	G01	6.6	0.34	5	1

[a] The off-axis angle is computed from the barycentre of the optical axes of the three telescopes using XMMSAS variables XCEN YCEN weighted by the mean detector sensitivity (see Pacaud et al. 2006). [b] Only galaxies within a projected distance <500 kpc of the cluster centre are counted. [c] Listed by Andreon et al. (2005). [d] Already published by Valtchanov et al. (2004). [e] Already published by Willis et al. (2005).

templates within the IRAF procedure xcsao (Kurtz & Mink 1998) and confirmed via visual inspection. A more detailed description of the spectroscopic techniques employed by the *XMM*-LSS survey can be found in Valtchanov et al. (2004) and Willis et al. (2005). In addition to the above spectroscopic observations, cluster redshift information was supplemented where available by spectra contributed from the VVDS (see Table 3).

The D1 X-ray clusters with confirmed redshifts are presented in Table 3. C1 and C2 confirmed clusters constitute a controlled sample (following Section 2.3) and are associated with the label 'XLSSC' and a three digit identifier.[6] This nomenclature is used to identify individual clusters in any later discussion. The completeness of C3 sources is not addressed. In the case where a particular cluster is present in two separate *XMM* pointings, only the pointing where the cluster is the closest to the optical centre has been used to measure its properties. Note that the off-axis restriction imposed on the C3 clusters excludes two faint clusters located at the very border of the D1 area and reported in the Willis et al. (2005) initial sample (XLSSUJ022633.9−040348, XLSSUJ022628.2−045948). Cluster redshift values given in Table 3 are the unweighed mean of relatively small member samples and observed, in a few cases, using different spectrographs. As this approach may result in relatively large (several hundred km s^{-1}) uncertainties in the computed redshift, the cluster redshift precision reported in Table 3 has been set to two decimal points (3000 km s^{-1}). X-ray/optical overlays of each cluster field are displayed in Fig. B1.

3 X-RAY PROPERTIES OF CONFIRMED CLUSTERS

The spectral and spatial X-ray data for each spectroscopically confirmed cluster were analysed to determine the temperature, spatial morphology and total bolometric luminosity of the X-ray emitting gas.

3.1 Spectral modelling and temperature determination

A complete description of the spectral extraction and analysis procedures as applied to X-ray sources with low signal levels using the XSPEC package (Arnaud 1996), together with a discussion on the accuracy of the computed temperatures, are presented in Willis et al. (2005). We summarize the principal steps below.

Spectral data were extracted within an aperture of specified radius (see Table 4) and a corresponding background region was defined by a surrounding annulus. Photons were extracted over the energy range [0.3–10] keV, excluding the energy range [7.5–8.5] keV due to emission features produced by the pn detector support. Analyses of

---

[6] The acronym is defined at CDS at the following URL http://vizier.u-strasbg.fr/cgi-bin/Dic?XLSSC.

Table 4. Spectral X-ray parameters. The radius of the circular aperture used for the spectral extraction is denoted by R_{spec}. Computed source counts are summed over the three detectors. The suffix 'F' applied to temperature values indicates that a reliable temperature fit was not achieved and a gas temperature of 1.5 keV was assumed for the computation of bolometric luminosity.

Cluster	R_{spec} (arcscec)	Source counts in R_{spec} [0.3–7.5]+[8.5–10] keV	T (keV)	C-statistics (per degree of freedom)	r_{500} (Mpc)	(arcsec)
XLSSC 029	33	311	$4.1^{+1.7}_{-1.0}$	1.08	0.52	67
XLSSC 044	55	234	$1.3^{+0.2}_{-0.2}$	1.15	0.40	100
XLSSC 025	35	661	$2.0^{+0.5}_{-0.3}$	1.06	0.53	129
XLSSC 041	45	523	$1.3^{+0.3}_{-0.1}$	1.00	0.43	172
XLSSC 011	68	425	$0.6^{+0.2}_{-0.1}$	1.04	0.28	272
XLSSC 005	35	164	$3.7^{+3.5}_{-1.4}$	1.02	0.49	60
XLSSC 013	30	161	$1.0^{+0.2}_{-0.2}$	0.92	0.33	73
XLSSC 022	39	1304	$1.7^{+0.2}_{-0.2}$	0.91	0.47	109
XLSSC 038	33	118	1.5F	–	0.37	56
cluster a	24	160	1.5F	–	0.40	69
cluster b	30	<100	1.5F	–	0.30	38
cluster c	30	<100	1.5F	–	0.32	42
cluster d	25	157	$0.9^{+0.2}_{-0.2}$	0.74	0.31	65

simulated spectral data with less than 400 total counts indicated that using C-statistics on unbinned spectral data produced a systematic offset in the computed temperature. This bias is significantly reduced for such faint spectra when the data are resampled such that at least five photons are present in each spectral bin corresponding to the background spectrum. We determined that this approach produces reliable temperature measures for low temperature ($T < 3$ keV), low count level (<400 photons) spectral data. The assumed fitting model employs an absorbed APEC plasma (Smith et al. 2001) with a fixed metal abundance ratio given by Grevesse & Sauval (1999) and set to 0.3 of the solar value. Absorption due to the Galaxy is modelled using the WABS function (Morrison & McCammon 1983), fixing the hydrogen column density to the value given by Dickey & Lockman (1990) at the cluster position (typically $\sim 2.6 \times 10^{20}$ cm^{-2}). Where the temperature fitting procedure failed to converge to a sensible model (due to low signal levels), the source temperature was fixed at 1.5 keV. Results of the X-ray spectral analysis are presented in Table 4. An example of cluster spectrum and fit is shown in Fig. 2.

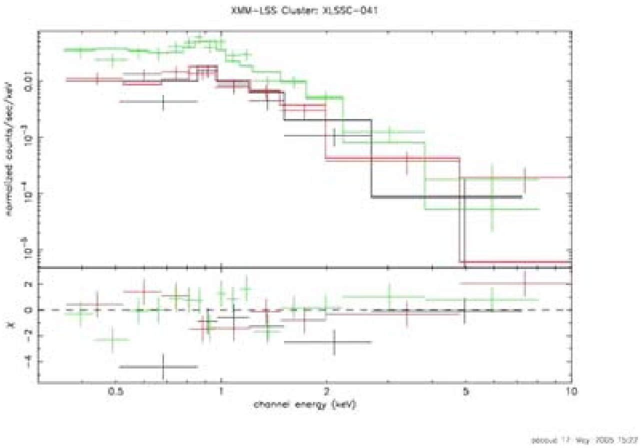

Figure 2. Fitted spectrum and residuals for cluster XLSSC 041 (MOS1: black, MOS2: red, pn: green).

3.2 Source morphology and spatial modelling

Sources detected using XAMIN are initially compared to two surface brightness models describing the two-dimensional photon distribution: a point source and a circular β-profile of the form

$$S(r) = \frac{A}{\left[1 + (r/R_{\mathrm{c}})^2\right]^{3\beta - 1/2}}, \tag{1}$$

where $\beta = 2/3$ is fixed while the core radius, R_{c}, and profile normalization, A, are permitted to vary (Cavaliere & Fusco-Femiano 1976). Each profile is convolved with the mean analytical PSF at the corresponding off-axis location and a comparison of the statistical merit achieved by each profile provides an effective discriminator of point and extended sources in addition to an initial estimate of the source flux (see Pacaud et al. 2006).

The photometric reliability of this procedure when applied to faint, extended sources is affected by the presence both of gaps in the *XMM* CCD array and by nearby sources (although both are described within the fitting procedure) – largely due to variations in the true source morphology and the fact that a larger fraction of the total emission is masked by the background when compared to brighter sources. Although such effects are naturally incorporated into the selection function appropriate for each cluster class via simulations (Pacaud et al. 2006), a further interactive spatial analysis was performed on each spectroscopically confirmed cluster in order to optimize the measure of the total emission (i.e. flux and luminosity) within a specified physical scale.

The photon distribution for each confirmed cluster is modelled using a one-dimensional circular β-profile in which β, R_{c} and A are permitted to vary. Photons from the three *XMM* detectors are co-added applying a weight derived from the relevant exposure map and pixels associated with nearby sources are excluded. Photons are binned in concentric annuli of width 3 arcsec centred on the cluster X-ray emission. Radial data bins are subsequently resampled to generate a minimum S/N > 3 per interval. The background is computed at large radius assuming a constant particle contribution plus vignetted cosmic emission. The above resampling procedure is then applied to the circular β-profile convolved with the mean analytical PSF[7] computed at the corresponding cluster off-axis angle (Ghizzardi 2002). Model cluster profiles are realized in this manner over a discrete grid of β and R_c values with the best-fitting model for each cluster determined by minimizing the χ^2 statistic over the parameter grid. Finally, the best-fitting spatial profile (at this point in units of photon count rate) is integrated out to a specified physical radius and converted into flux and luminosity units using standard procedures within XSPEC.

The majority of confirmed clusters are apparently faint, displaying total photon counts of order a few hundred, and the observed photon distribution in many cases represents only a fraction of the extended X-ray surface brightness distribution. Under such conditions the parameters β and R_c are degenerate when fitted simultaneously, limiting the extent to which 'best-fitting' parameters can be viewed as a physically realistic measure of the cluster properties, although providing a useful ad hoc parametrization. For this reason we do not quote best-fitting values of β and R_c derived for each confirmed cluster. The uncertainty associated with the procedure is evaluated using a large suite of simulated observations (and subsequent analyses) of clusters of specified surface brightness properties (i.e. β, R_c and apparent brightness – Pacaud et al. in preparation). The fractional uncertainty can then be quoted as a function of the number of photons collected within the fitting radius $R_{\rm fit}$ (the maximum radius out to which the resampling criterion $S/N > 3$ was achieved) and the radius to which the profile is calculated (possibly, extrapolated). Note that, as shown in the next section, almost all clusters have $R_{\rm fit}$ greater than the physical integration radius, hence requiring no profile extrapolation. For the very faintest clusters (those with total photon counts less than ~100) a simple sum within a circular aperture was applied.

As an example of the above spatial fitting procedure, Fig. 3 shows the data analysis regions applied to the cluster XLSSC 041. Fig. 4 displays the resulting one-dimensional radial profile and the best-fitting surface brightness model for the same cluster.

3.3 Determination of cluster flux and luminosity

Values of flux and luminosity for confirmed clusters are obtained by integrating the cluster emission model, described by the appropriate XSPEC plasma emission and surface brightness models, out to a specified physical radius. We use a different physical radius for flux measures as opposed to luminosity – mainly because tabulated flux values for cluster surveys present in the literature prefer an estimate of the 'total' flux within a limited energy interval whereas luminosity values are computed as the bolometric emission within a physical radius corresponding to a constant overdensity in an evolving universe (e.g. r_{500}).

Flux values are computed by integrating the best-fitting β-profile to a radius of 500 kpc. The specified aperture includes a substantial fraction of the total flux (approximately 2/3 of the flux from β-profile described by $\beta = 2/3$ and $R_c = 180$ Mpc) yet avoids uncertainties associated with the extrapolation of the profile to large radii.

In order to obtain cluster luminosities within a uniform physical radius, we have integrated the best-fitting β-profile for each cluster to r_{500}, that is, the radius at which the cluster mass density reaches 500 times the critical density of the Universe at the cluster redshift. Values of r_{500} for each cluster were computed using the mass–temperature data of Finoguenov, Reiprich & Böhringer (2001) which, when converted to our assumed cosmology and fitted with an orthogonal regression line, yield the expression $r_{500} = 0.391\, T^{0.63}\, h_{70}(z)^{-1}$ Mpc for clusters in the $0.7 < T < 14$ keV interval. As reported in Willis et al. (2005), values of r_{500} from this formula agree well with those derived from assuming an isothermal β-profile for clusters displaying $T \lesssim 4$ keV.

For each cluster in the confirmed sample, with the exception of XLSSC 005, the computed values of r_{500} lie within radius of, or close to, the region employed to fit the β-profile (hence, for this cluster alone, the photometric errors are large as reported in Table 5).

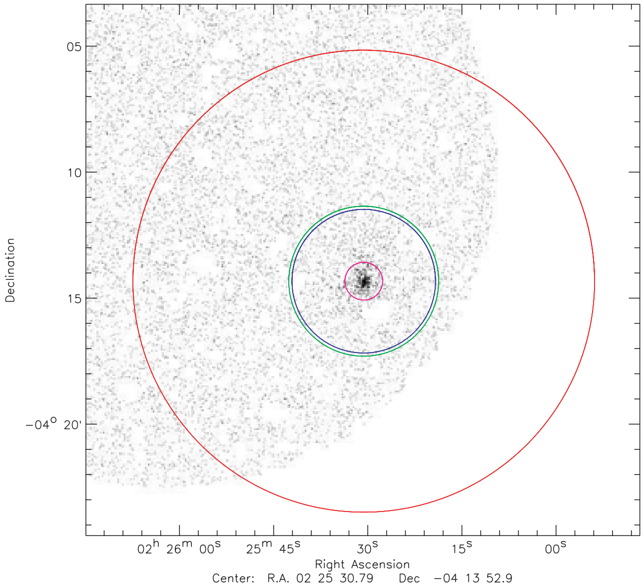

Figure 3. An example of the spatial and spectral analysis regions applied to cluster XLSSC 041. The photon image is displayed. The purple circle indicates the spectral extraction region. The green circle indicates r_{500}. The blue circle indicates $R_{3\sigma} = R_{\rm fit}$. All X-ray sources, except the cluster of interest, are masked. The external red circle delineates the region used for the fit.

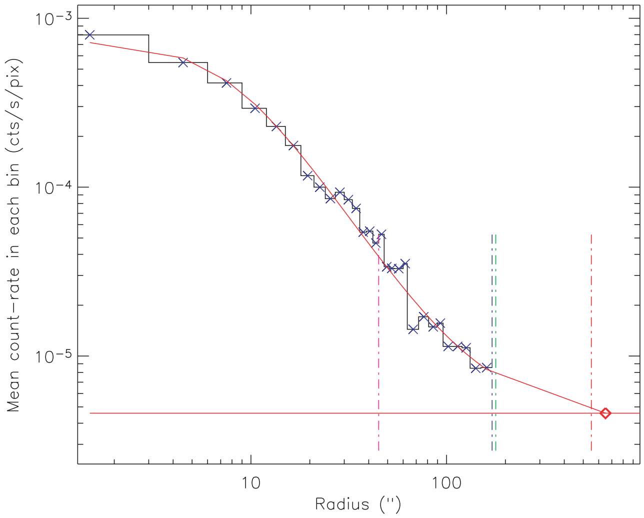

Figure 4. The radially averaged X-ray emission profile for cluster XLSSC 041. The red curve indicates the best-fitting model compared to the data (black histogram with blue crosses). The vertical lines follow the same colour coding as Fig. 3. The red horizontal line marks the background level.

---

[7] The convolution of the two profiles models the photon distribution factor introduced by the two-dimensional convolution (Arnaud et al. 2002).

Table 5. Results of the spatial analysis for confirmed clusters. See text for the definition of the fitting radius R_{fit}. The net source counts are computed within R_{fit} and are uncorrected for vignetting. A value of 'NF' indicates that no reliable spatial fit was possible for the cluster: the source counts, flux and luminosity were computed applying a circular aperture of radius 500 kpc. Flux values are computed by integrating the best-fitting cluster β-profile out to a radius of 500 kpc. The photometric precision indicates the mean 1σ errors estimated from analyses of simulated cluster data and accounts for the profile fitting uncertainties only (see text for details).

Cluster	R_{fit} (arcsec)	Source counts in R_{fit} in [0.5–2] keV	$F_{[0.5-2]}$ (10^{-14} erg s^{-1} cm^{-2})	$L_{\mathrm{bol}}(r_{500})$ (10^{44} erg s^{-1})	Photometric accuracy (per cent)
XLSSC 029	60	361	3.1	4.8	20
XLSSC 044	129	318	2.5	0.11	15
XLSSC 025	123	905	9.4	0.52	15
XLSSC 041	171	819	20.6	0.24	15
XLSSC 011	354	972	16.4	0.015	15
XLSSC 005	39	128	1.1	1.5	60
XLSSC 013	234	383	2.7	0.15	20
XLSSC 022	171	1785	9.8	0.65	10
XLSSC 038	NF	[60]	0.3	0.09	–
cluster a	NF	[108]	0.7	0.1	–
cluster b	NF	[52]	0.4	0.4	–
cluster c	NF	[29]	0.3	0.3	–
cluster d	432	417	0.83	0.078	20

Bolometric X-ray luminosities were calculated for each cluster by extrapolating the APEC plasma code corresponding to the best-fitting temperature to an energy of 50 keV. Values of r_{500}, flux and luminosity for each confirmed cluster are listed in Tables 4 and 5.

In Appendix A, we analyse the impact of further sources of uncertainty affecting the luminosity and temperature measurements.

Appendix B gathers notes on the individual clusters and investigate, among others, the possibility that the computed clusters brightness values may be contaminated by AGN emission. We conclude that none of the C1 and C2 clusters (i.e. those used for detailed population statistics) contained in the D1 sample are significantly contaminated by AGN emission.

3.4 Trends in the L_{X} versus T_{X} correlation

Fig. 5 displays the L_{X} versus T_{X} distribution of the D1 clusters for which it was possible to measure a temperature (eight C1 and one C3 objects). Although the D1 area represents only a subset of the anticipated *XMM*-LSS area, the C1 sample is complete and reliable temperature information is available for all systems. It is therefore instructive to consider trends in the L_{X} versus T_{X} distribution in anticipation of a larger sample of C1 clusters from the continuing survey. The location of C1 clusters in the L_{X} versus T_{X} plane is compared to a regression line computed for a combined sample of local sources based upon the group data of Osmond & Ponman (2004) and cluster data of Markevitch (1998). The computed regression line takes the form, $\log L_{\mathrm{X}} = 2.91 \log T_{\mathrm{X}} + 42.54$, for bolometric luminosity computed within r_{500}. A complete discussion of the regression fit will be presented by Helsdon & Ponman (in preparation).

One issue of interest concerns the properties of intermediate redshift ($z \sim 0.3$) X-ray groups (i.e. $T_{\mathrm{X}} \sim 1$–2 keV). Such systems dominate the *XMM*-LSS numerically and, when compared to higher temperature, higher mass clusters, are expected to demonstrate to a greater degree the effects of non-gravitational physics in the evolution of their X-ray scaling relations with respect to self-similar evolution models. The luminosity of X-ray sources in *XMM*-LSS may be compared to those of local sources at the same temperature by computing the luminosity enhancement factor, $F = L_{\mathrm{obs}}/L_{\mathrm{pred}}$, where L_{obs} is the observed cluster X-ray luminosity within a radius, r_{500}, and L_{pred} is the luminosity expected applying the fitted L_{X} versus T_{X} relation computed for the local sources and the *XMM*-LSS measured temperature. Sources XLSSC 013, 022 and 041 have a luminosity enhancement factors $F \approx 3$–4, compared to a value 1.15 expected from self-similar[8] luminosity scaling within r_{500}.

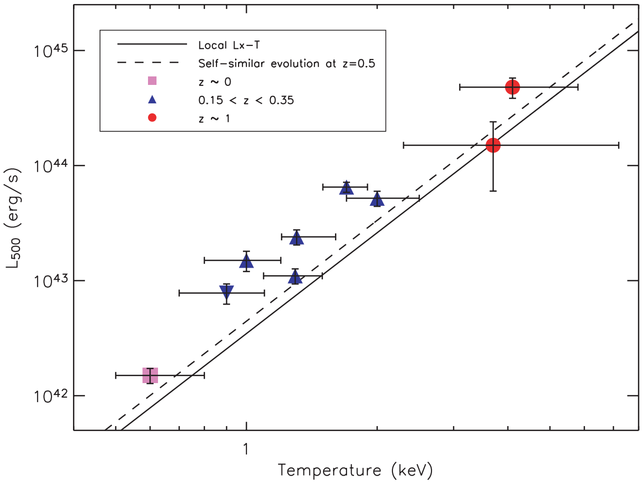

Figure 5. $L_{\mathrm{X}}(r_{500})$ versus T_{X} relation for the clusters for which it was possible to derive a temperature; all of them but *cluster d* (displayed as an upside-down triangle) are C1. The solid line gives the mean local $L_{\mathrm{X}} - T_{\mathrm{X}}$ relation (see text), while the dotted line is the expected luminosity enhancement assuming self-similar luminosity scaling within r_{500} at $z = 0.5$. Different plotting symbols indicate clusters located within three different redshift intervals.

From the local Universe, we know that low-temperature groups show a larger dispersion in the L–T relation than massive clusters (Helsdon & Ponman 2003). This reflects their individual formation histories, since they are particularly affected by non-gravitational effects, as well as the possible contributions from their member

---

[8] Self-similar implies that the luminosity scales as the Hubble constant when integrated within a radius corresponding to a fixed ratio with respect to the critical density of the Universe as a function of redshift (Voit 2005).

galaxies. The apparent biasing towards more luminous objects and/or cooler system could come from the fact that we detect more easily objects having a central cusp, that is, putative cool-core groups. This has the effect of both decreasing the temperature and increasing the luminosity. The bias could also simply reflect the fact that we can measure a temperature only for the brightest objects.

In order to test this hypothesis, we have considered a few orders of magnitude. The local L–T relation predicts a luminosity of 1.1×10^{43} and 2.6×10^{43} erg s^{-1} for $T = 1.5$ and 2 keV groups, respectively. A factor of 2 under luminosity for such objects would thus correspond to 5.6×10^{42} and 1.3×10^{43} erg s^{-1}. In Table 5, we note that (i) the lowest flux cluster (XLSSC 005) is detected with some 150 photons in R_{fit}; the X-ray image appears moreover to be quite flat; (ii) group XLSSC 044 ($z = 0.26$) has a luminosity of 1.1×10^{43} erg s^{-1}, for some 300 photons in R_{fit}. From this, we infer that we could have detected groups around $z \sim 0.25$, having $1.5 < T < 2$ keV that are under luminous by a factor of 2, if any were present in our sample. Below 1.5 keV, these objects are likely to remain undetected.

The coming availability of the larger *XMM*-LSS sample will permit a more reliable assessment of such effects on the morphology–luminosity–temperature plane for such groups (Pacaud et al. in preparation).

4 DISCUSSION AND CONCLUSION

We have used 20 ks *XMM* images to construct a deep sample of galaxy clusters. The total cluster surface density of 15.5 deg^{-2} is approximately five times larger than achieved previously with the deepest *ROSAT* cluster surveys (e.g. RDCS, Borgani et al. 2001). On the one hand, from the optical point of view, we note that none of the detected clusters shows strong lensing features, hence the likely absence of massive clusters in the D1 area.[9] This is consistent with the fact that the highest cluster X-ray temperature is only 4 keV: this temperature corresponds to a mass of $\sim 3 \times 10^{14}$ M$_{\odot}$ and, in a standard Lambda cold dark matter halo model (Pacaud et al. 2006), the density of clusters more massive than this limit, that is, those most likely to produce strong lensing, is $\sim$0.8 deg^{-2}. On the other hand, it is indeed a salient property of the *XMM*-LSS to unveil for the first time the bulk of the $1 < T < 2$ keV group population in the $0.1 < z < 0.4$ range along with its capability of detecting $z \geqslant 1$ clusters. We further review below the main properties of the sample.

The C1 cluster subsample corresponds to a purely X-ray selected sample (zero contamination) and displays a surface density of $\sim$9 deg^{-2}. Reliable temperature information is available for all C1 sources and optical spectroscopic observations are required only to confirm the cluster redshift. Relaxing the selection criteria used to generate the C1 sample creates additional samples labelled C2 and C3. However, optical imaging and spectroscopic data are required to identify bona fide clusters within these samples. The C2 sample possesses a well-defined X-ray selection function (approximately 50 per cent of sources are confirmed as clusters) and the surface density of C1 + C2 clusters is $\sim$11 deg^{-2}. Sources labelled C3 represent significant detections out with the C1 and C2 selection criteria and, given the high contamination rate, we do not compute a selection function for these sources. The C3 sample contains potentially interesting objects and points to our ultimate sensitivity for cluster detection which appears to be around 5×10^{-15} erg s^{-1} cm^{-2}; however, we stress that the full selection function for the C1 and C2 samples is multidimensional (see below). Noting this caveat – for comparison purposes only – the quoted flux sensitivity corresponds to a cluster of $\sim 7 \times 10^{43}$ erg s^{-1} ($T \sim 3$ keV) at $z = 1$ and to a group of 3.5×10^{42} erg s^{-1} ($T = 1$ keV) at $z = 0.3$. We further note that no C1 or C2 cluster emission appears to be significantly contaminated by AGN activity – partly a result of the high threshold put on the extent likelihood for these samples.

Having the D1 *XMM*-LSS sample now assembled, it is instructive to examine in what manner it differs from a purely flux-limited sample. This question is phenomenologically addressed by Pacaud et al. (2006) as the answer depends on two major ingredients: (1) the pipeline efficiency (involving itself the many instrumental effects) – this is quantified by means of extensive simulations; (2) the characteristics of the cluster population out to a redshift of unity at least – this latter point being especially delicate as the low-end of the cluster mass function, critical for the survey sensitivity, is poorly known and cluster scaling law evolution, still a matter of debate. Hence the need for a self-consistent approach basically involving a cosmological model, a halo mass spectrum and some $L_{\mathrm{X}}(M, T, R_{\mathrm{c}}, z)$ function[10] describing the evolution of the cluster intrinsic properties that directly impact on the cluster detection efficiency. The principal conclusion regarding the use of a single flux limit is that, to obtain a cluster sample displaying a high level of completeness and reasonably low contamination, the flux limit has to be set to some high value, for example, $F > 5 \times 10^{-14}$ erg s^{-1} cm^{-2} in the case of *XMM*-LSS. The present study demonstrates on real data the advantage of using the C1 set of criteria as a well-defined sample that includes groups down to $T = 1$ keV and fluxes as low as 10^{-14} erg s^{-1} cm^{-2} and, consequently, significantly increases the size of the purely X-ray selected sample. Although the C1 criteria, even fully controlled, might at first sight appear more pipeline dependent and, thus, less physical than a simple flux limit, we stress that any X-ray detection algorithm is bound to miss low luminosity clusters in a way that is pipeline dependent – the loss of efficiency not being a simple flux limit. For these reasons, we favour the concept of *controlled sample* (in the C1 selection sense) rather than of *complete flux-limited sample*.

Our D1 sample contains seven clusters displaying a flux in excess of 2×10^{-14} erg s^{-1} cm^{-2} (all C1). This corresponds to a surface density of $\sim$8 deg^{-2} and is larger than the 4–5 clusters deg^{-2} implied by the RDCS log N–log S relation (Rosati et al. 1998) – the only *ROSAT* cluster sample complete to 2×10^{-14} erg s^{-1} cm^{-2} (Rosati et al. 2002) – in addition to the shallow *XMM*/2dF survey (Gaga et al. 2005), reporting 7/2.3 = 3 deg^{-2} at the same flux limit. The probability to obtain 8 clusters deg^{-2} from the RDCS number density is 1–10 per cent, assuming simple Poisson statistics. Given the relatively small fields covered in each case, the effects of cosmic variance upon any such comparison may well be important (the *XMM*/2dF survey and deepest regions of the RDCS cover 2.3 and 5 deg^{2}, respectively). For comparison, the simple cluster evolution plus cosmological model presented by Pacaud et al. (2006) predicts a surface density of $\sim$7.5 clusters deg^{-2} displaying $T > 1$ keV and a flux $F > 2 \times 10^{-14}$ erg s^{-1} cm^{-2}.

We have computed reliable temperature values for nine of the 13 confirmed clusters – in particular, the C1 sample is 'temperature'

---

[9] With the caveat that the presence of giant arcs requires not only a large mass concentration but also a specific lens/source configuration.

[10] The function is normalized from local Universe observations and its evolution constrained by available high-z data, numerical simulations and other possible prescriptions such as self-similarity evolution; one of the main unknowns being the role of non-gravitational physics in cluster evolution.

complete. This is important as it displays the potential for survey quality *XMM* observations to investigate the evolution of X-ray (and additional waveband) cluster scaling relations in a statistical manner over a wide, uniformly selected redshift interval. Together with the initial sample presented by Willis et al. (2005), the D1 sample is the first sample to investigate the L_X versus T_X relation for $1 < T < 2$ keV groups at $0.15 < z < 0.35$, for the simple reason that this population was previously undetected. *XMM*-LSS therefore samples a relatively complete, high surface density population of clusters displaying temperatures $T > 1$ keV at redshifts $z \lesssim 1$ and provides an important new perspective for the study the cluster and group evolution employing only moderate *XMM* exposure times.

All data presented in this paper – cluster images taken at X-ray and optical wavebands in addition to detailed results for the spectral and spatial analyses – are available in electronic form at the *XMM*-LSS cluster online data base: http://l3sdb.in2p3.fr:8080/l3sdb/login.jsp.

ACKNOWLEDGMENTS

We are grateful to M. Arnaud for providing her profile convolution routine. We thank J. Ballet, R. Gastaud and J.-L. Sauvageot for useful discussions. AG acknowledges a CNES CDD position. GG and HQ thank the support of the FONDAP Centre for Astrophysics # 15010003. SA acknowledges financial contribution from contract ASI-INAF I/023/05/0. The results presented here are based on observations obtained with *XMM–Newton*, an ESA science mission with instruments and contributions directly funded by ESA Member States and NASA. The cluster optical images were obtained with MegaPrime/MegaCam, a joint project of CFHT and CEA/DAPNIA, at the CFHT which is operated by the National Research Council (NRC) of Canada, the Institut National des Sciences de l'Univers of the Centre National de la Recherche Scientifique (CNRS) of France and the University of Hawaii. This work is based in part on data products produced at TERAPIX and at the Canadian Astronomy Data Centre as part of the CFHTLS, a collaborative project of NRC and CNRS.

REFERENCES

Andreon S., Valtchanov I., Jones L. R., Altieri B., Bremer M., Willis J., Pierre M., Quintana H., 2005, MNRAS, 359, 1250
Arnaud K. A., 1996, in Jacoby G. H., Barnes J., eds, ASP Conf. Ser. Vol. 101, Astronomical Data Analysis Software and Systems V. Astron. Soc. Pac., San Francisco, p. 17
Arnaud M., Majerowicz S., Lumb D., Neumann D. M., 2002, A&A, 390, 27
Arnaud M., Pointecouteau E., Pratt G. W., 2005, A&A, 441, 893
Böhringer H. et al., 2000, ApJS, 129, 435
Böhringer H. et al., 2001, A&A, 369, 826
Bondi M. et al., 2003, A&A, 403, 857
Borgani S. et al., 2001, ApJ, 561, 13
Burke D. J., Collins C. A., Sharples R. M., Romer A. K., Holden B. P., Nichol R. C., 1997, ApJ, 488, L83
Cavaliere A., Fusco-Femiano R., 1976, A&A, 49, 137
Chiappetti L. et al., 2005, A&A, 439, 413
Dickey J. M., Lockman F. J., 1990, ARA&A, 28, 215
Finoguenov A., Reiprich T. H., Böhringer H., 2001, A&A, 368, 749
Gaga T., Plionis M., Basilakos S., Georgantopoulos I., Georgakakis A., 2005, MNRAS, 363, 811
Ghizzardi S., 2002, *XMM*-SOC-CAL-022 & 029
Grevesse N., Sauval A. J., 1999, A&A, 347, 348
Helsdon S. F., Ponman T. J., 2003, MNRAS, 340, 485
Henry J. P., Gioia I. M., Mullis C. R., Voges W., Briel U. G., Böhringer H., Huchra J. P., 2001, ApJ, 553, L109
Ilbert O. et al., 2005, A&A, 439, 863
Kurtz M. J., Mink D. J., 1998, PASP, 110, 934
Markevitch M., 1998, ApJ, 504, 27
Moretti A., Campana S., Lazzati D., Tagliaferri G., 2003, ApJ, 588, 696
Moretti A. et al., 2004, A&A, 428, 21
Morrison R., McCammon D., 1983, ApJ, 270, 119
Osmond J. P. F., Ponman T. J., 2004, MNRAS, 350, 1511
Pacaud F., Pierre M. et al., 2006, MNRAS, in press (doi:10.1111/j.1365-2966.2006.10881.x) (this issue)
Pierre M. et al., 2004, J. Cosmology Astropart. Phys., 9, 11
Pratt G. W., Arnaud M., 2002, A&A, 394, 375
Rapetti D., Allen S. W., Weller J., 2005, MNRAS, 360, 555
Romer A. K. et al., 2000, ApJS, 126, 209
Rosati P., della Ceca R., Norman C., Giacconi R., 1998, ApJ, 492, L21
Rosati P., Borgani S., Norman C., 2002, ARA&A, 40, 539
Scharf C., 2002, ApJ, 572, 157
Smith R. K., Brickhouse N. S., Liedahl D. A., Raymond J. C., 2001, ApJ, 556, L91
Valtchanov I., Pierre M., Gastaud R., 2001, A&A, 370, 689
Valtchanov I. et al., 2004, A&A, 423, 75
Vikhlinin A., McNamara B. R., Forman W., Jones C., Quintana H., Hornstrup A., 1998, ApJ, 498, L21
Voit M., 2005, Rev. Mod. Phys., 77, 207
Willis J. P. et al., 2005, MNRAS, 363, 675

APPENDIX A: ERROR BUDGET ON THE CLUSTER LUMINOSITY AND TEMPERATURE MEASUREMENTS

This appendix investigates the impact of specific sources of uncertainty on the cluster temperature and flux measurements. The calculations are performed for three clusters representative of the flux and temperature ranges covered by the present sample, namely XLSSC 41, 29, 13.

(1) Cluster luminosities are computed within r_{500}, a quantity empirically derived from the temperature (Section 3.3), while the photometric errors quoted in Table 5 results from the spatial fit only. In Table A1 we provide the uncertainty on the luminosity induced by the errors from the temperature measurements, as propagated through the derivation of r_{500} (the spatial fit is then assumed to be exact). The results show that they are negligible compared to the accuracy level of the spatial fits.

(2) Cluster temperatures are estimated fixing the metal abundance to 0.3 solar (Section 3.1). Since many of our clusters have $T < 2$ keV, for which the contribution from emission lines is significant, some temperature-abundance degeneracy could occur in the spectral fitting – all the more so since the number of photons involved in the spectral fit is small. In Table A1 we provide further temperature measurements fixing the abundance to 0.1 or 0.6 solar. The results show that the impact on the derivation of the temperature and associated errors is negligible. In all these trials, the Galactic column density is held fixed.

(3) Finally, we investigate whether the contribution of unresolved AGNs to the integrated cluster emission is statistically significant at our sensitivity. We proceed here assuming the *XMM* $\log N$–$\log S$ for point sources (Moretti et al. 2003) since no information on the AGN environment of low-luminosity clusters is available to date. For each ring of the cluster spatial profile, we compute the limiting flux for which a point source is to be detected at the 3σ level. We then integrate the $\log N$–$\log S$ over the cluster area out to $R = 500$ kpc, between the varying flux limit and the background flux level. Results are gathered in Table A1 and show that, statistically, the point source contribution is negligible. In Appendix B we further inspect, for each cluster, the possibility that the core of the cluster emission could be contaminated by an AGN.

Table A1. Error budget for secondary effects. r_{500}^{-} and r_{500}^{+} are the extreme possible values for r_{500} derived from the temperature uncertainties quoted in Table 4.

XLSSC	41	29	13
source counts in $R_{\rm fit}, R_{\rm spec}$	819, 523	361, 311	383, 161
$r_{500}^{-}, r_{500}, r_{500}^{+}$	171, 179, 196 arcsec	66, 55, 82 arcsec	76, 69, 84 arcsec
$\frac{L_{\rm X}(r_{500}^{-/+})-L_{\rm X}(r_{500})}{L_{\rm X}(r_{500})}$	−2 per cent /+ 4 per cent	−1 per cent/+ 0.6 per cent	−5 per cent/+ 6 per cent
Ab = 0.1	$T = 1.3$ (1.1, 1.5) keV	$T = 4.2$ (3.1, 6.1) keV	$T = 1.0$ (0.8, 1.2) keV
Ab = 0.3	$T = 1.3$ (1.2, 1.6) keV	$T = 4.1$ (3.0, 5.8) keV	$T = 1.0$ (0.9, 1.2) keV
Ab = 0.6	$T = 1.5$ (1.3, 1.7) keV	$T = 4.0$ (3.0, 5.5) keV	$T = 1.0$ (0.9, 1.3) keV
Undetected AGN contribution $R < 500$ kpc	0.6 per cent	0.5 per cent	0.8 per cent

APPENDIX B: NOTES ON INDIVIDUAL CLUSTERS

In this appendix, we provide additional information for confirmed clusters. We have paid particular attention to whether the X-ray spectra and spatial emission of each cluster displays evidence for contamination by AGN emission. For each cluster we have compared the results generated by fitting the spatial emission having either included or excluded the central radial bin (radius of 3 or 6 arcsec). Although in some cases the best-fitting values of β and $R_{\rm c}$ varied significantly, in all cases the integrated count rate within r_{500} showed variations less than 10 per cent. The small number of photons contributed by the central few arcsec of each cluster prevented a separate spectral analysis of the central regions. Finally, we have investigated all examples of spatial coincidence between radio sources presented in Bondi et al. (2003) and the D1 cluster sample. We discuss individual clusters below.

In parallel, we have discovered a point-like source, XLSS J022528.2−041536, which is associated, at least in projection, with a group at redshift $z \sim 0.55$ (more than five concordant redshifts). However, the group emission, which is embedded in that of XLSSC 041, appears totally dominated by the point source and consequently, this object does not enter the C1 or C2 or C3 classes. A radio source ($S_{\rm tot} = 0.28$ mJy, ∼ 5 arcsec extent) is present at 2 arcsec from the X-ray centre. XLSS J022528.2−041536 is located in the field of XLSSC 041 and the group member galaxies are indicated in the overlay of Fig. B1. In a further study involving optical, radio and IR data, we will assess the fraction of clusters that remain unclassified because of strong AGN contamination.

XLSSC 029 The presence of a radio source ($S_{\rm tot} = 1.5$ mJy, ∼ 2 arcsec extent) some 11 arcsec from the cluster centre might suggest that the X-ray emission is contaminated by an AGN. However, examination of a recent 100 ks *XMM* pointing on this object (obs 0210490101, PI L. Jones) shows that the astrometry of the original *XMM*-LSS survey image is correct within 1 arcsec, and does not reveal a secondary maximum coincident with the radio source.

XLSSC 044 This cluster is of very low surface brightness and displays elongated emission. Its X-ray morphology, galaxy distribution and temperature of ∼1 keV suggest a group in formation.

XLSSC 025 A weak radio source ($S_{\rm tot} = 1.0$ mJy, ∼5 arcsec extent) lies at the centre of the cluster emission, however, the central galaxy spectrum displays no strong emission lines (rest-frame wavelength interval 3000–6000 Å is sampled). The X-ray spatial profile is peaked yet exclusion of the central 3 arcsec radial bin, does not change significantly the fitted value of $R_{\rm c}$ (it changes from 5 to 6 arcsec while $\beta = 0.44$ remains constant). We thus exclude any strong contamination by a central AGN, and favour the cool-core hypothesis.

XLSSC 041 No radio source was identified within 30 arcsec of the cluster emission centroid.

XLSSC 011 The X-ray and optical appearance of this system are suggestive of a compact group of galaxies. All point sources within a radius of 350 arcsec have been removed from the spatial analysis. However, it was not possible to estimate the extent of any contribution from the central galaxy to the group emission.

XLSSC 005 No radio sources are identified within the projected area covered by the X-ray emission. This system displays double-peaked X-ray emission morphology, with each peak associated with a distinct velocity component. The photometric uncertainty for this system is large as less than 200 photons were available for the spatial fit which was limited to $R_{\rm fit} \sim r_{500}/2$. The system is further discussed in Valtchanov et al. (2004).

XLSSC 013 No radio sources are identified within 1 arcmin of the X-ray centroid. A bright X-ray point source is present at 1 arcmin distance yet does not affect the cluster classification procedure and the point source is removed from the subsequent spatial and spectral analysis.

XLSSC 022 The X-ray profile is peaked and here is a weak radio source within 2 arcsec of the X-ray emission centroid ($S_{\rm tot} = 0.15$ mJy, no extent). The spectrum of the central galaxy displays no significant emission features consistent with AGN activity. The cluster morphology is very similar to XLSSC 025 in that $R_{\rm c}$ and β values do not vary significantly depending upon the inclusion of the central bin in the spatial analysis. We therefore favour the cool-core hypothesis for this system.

cluster a The X-ray centroid coincides with a radio source ($S_{\rm tot} = 0.21$ mJy, no extent) within 2 arcsec. The optical spectrum obtained for this object is faint and did not allow us to secure its redshift; however, no emission line is apparent in the spectrum. The photometric redshift is 0.98, with a SBI starburst as best-fitting spectrum. The flux at 24 μm is 0.4 mJy which is rather high. This suggests that the coincidence between this red object and the X-ray centroid might be fortuitous, but the contamination by an active nucleus cannot be excluded.

cluster b An X-ray point source is located some 30 arcsec from the X-ray emission centroid and was subsequently removed from the spatial and spectral analyses.

cluster d A radio source is located within 3 arcsec of the X-ray emission centroid ($S_{\rm tot} = 0.08$ mJy, no extent). The optical spectrum of the central galaxy does not show significant emission features. With an extent of 2.5 arcsec and a extent likelihood = 21 this marginal source is classified as C3.

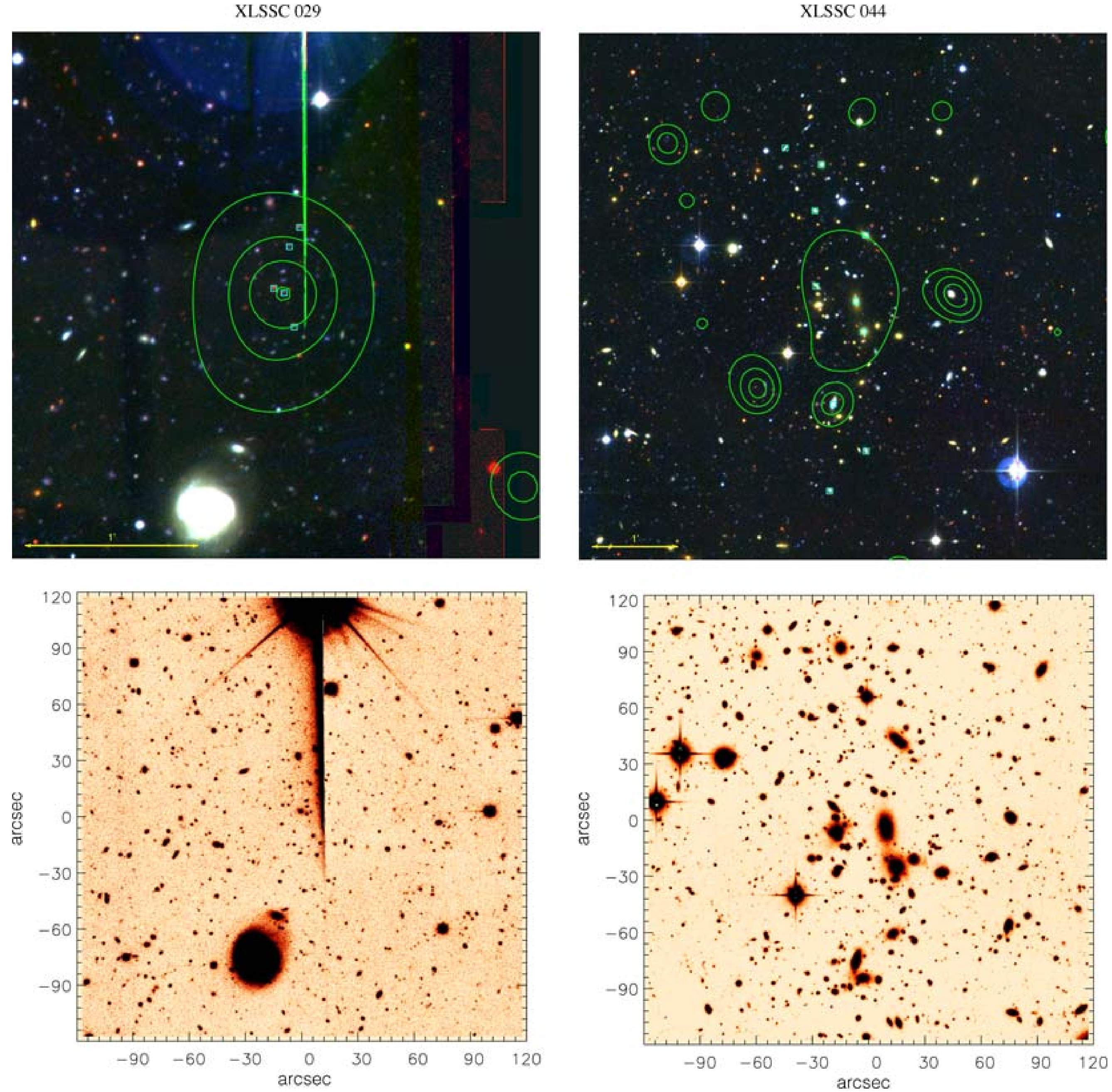

Figure B1. Colour overlays of the D1 clusters. Upper panel: cluster X-ray contours overlaid on a u, r, z CFHTLS composite. Contours are drawn from the co-added [0.5–2] keV MOS1 + MOS2 + pn mosaic filtered in the wavelet space using a significance threshold of 10^{-3} for Poisson statistics (not corrected for vignetting). The intensity scale is logarithmic and the same for all images; values are: 2.6e−06, 5e−06, 9.6e−06, 1.8e−05, 3.5e−05, 6.7e−05, 0.00013 counts pixel^{-1} s^{-1}. Boxes indicate galaxies whose redshift is in the $[z_{\rm cl} - 0.01, z_{\rm cl} + 0.01]$ range. The size of the images is 1.5 Mpc at the cluster redshift, except for the nearby group XLSSC011, for which the image is 0.6 Mpc aside. Lower panel: CFHTLS cluster I images, 4 arcmin aside.

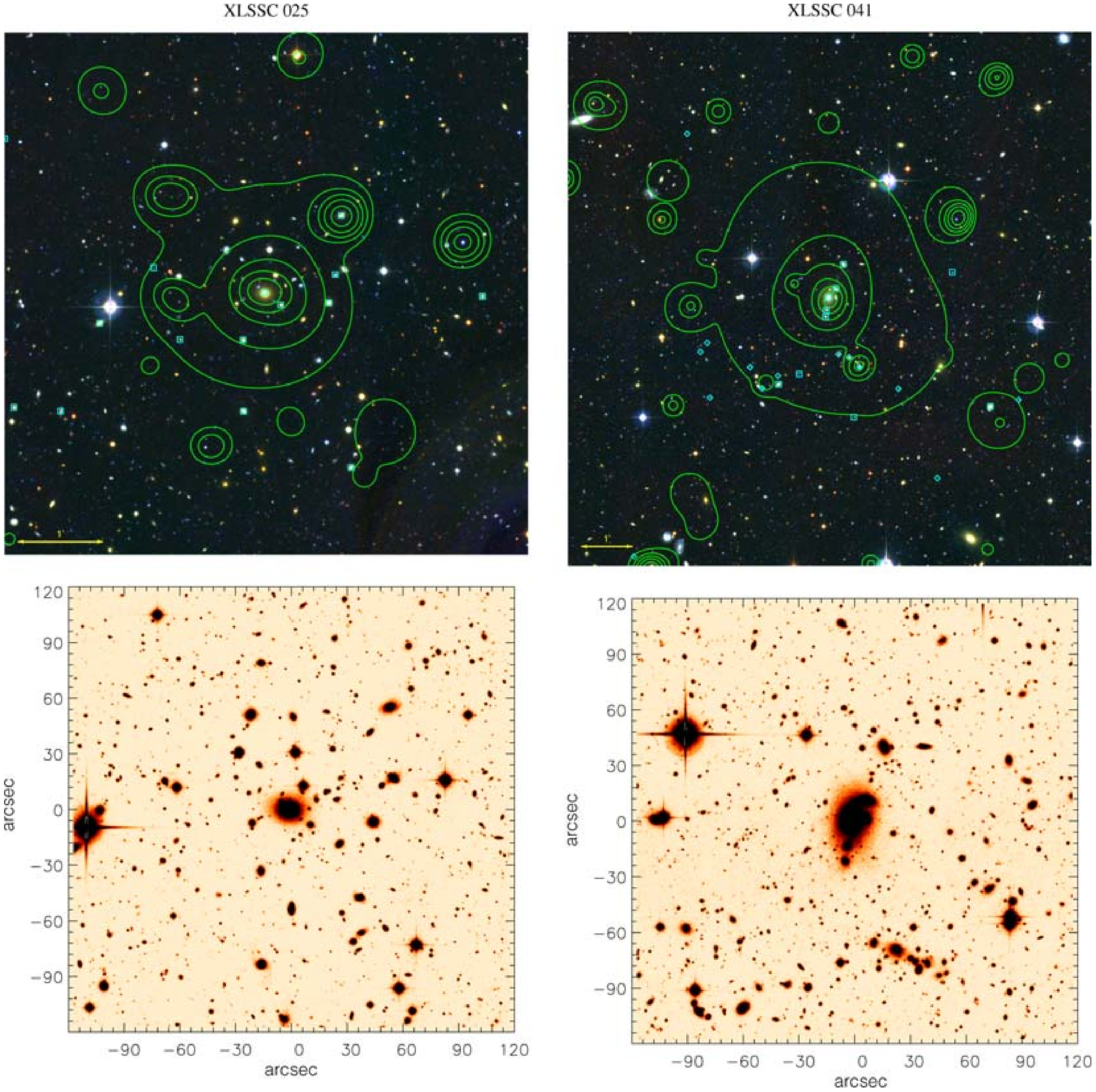

Figure B1 – *continued*

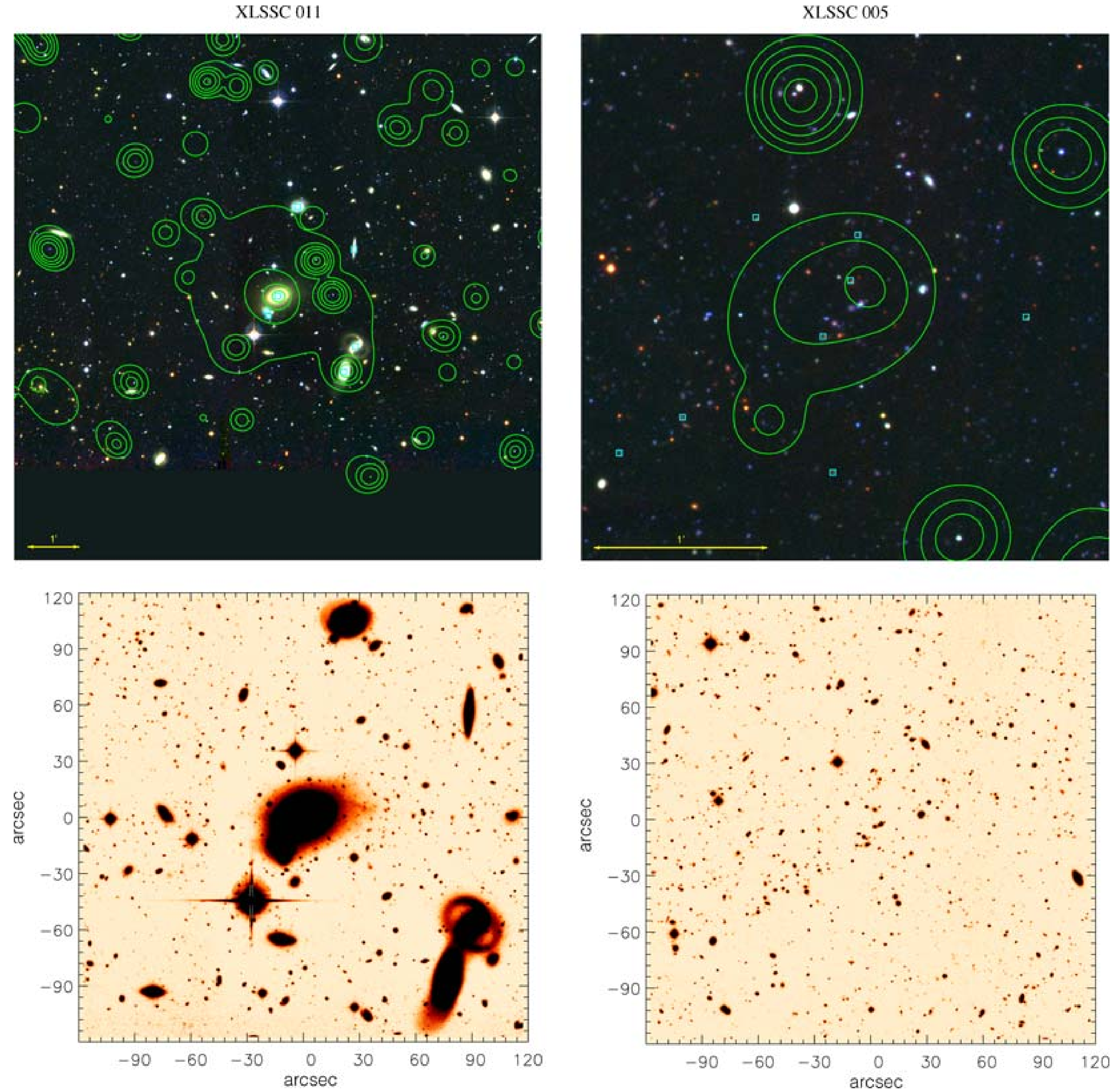

Figure B1 – *continued*

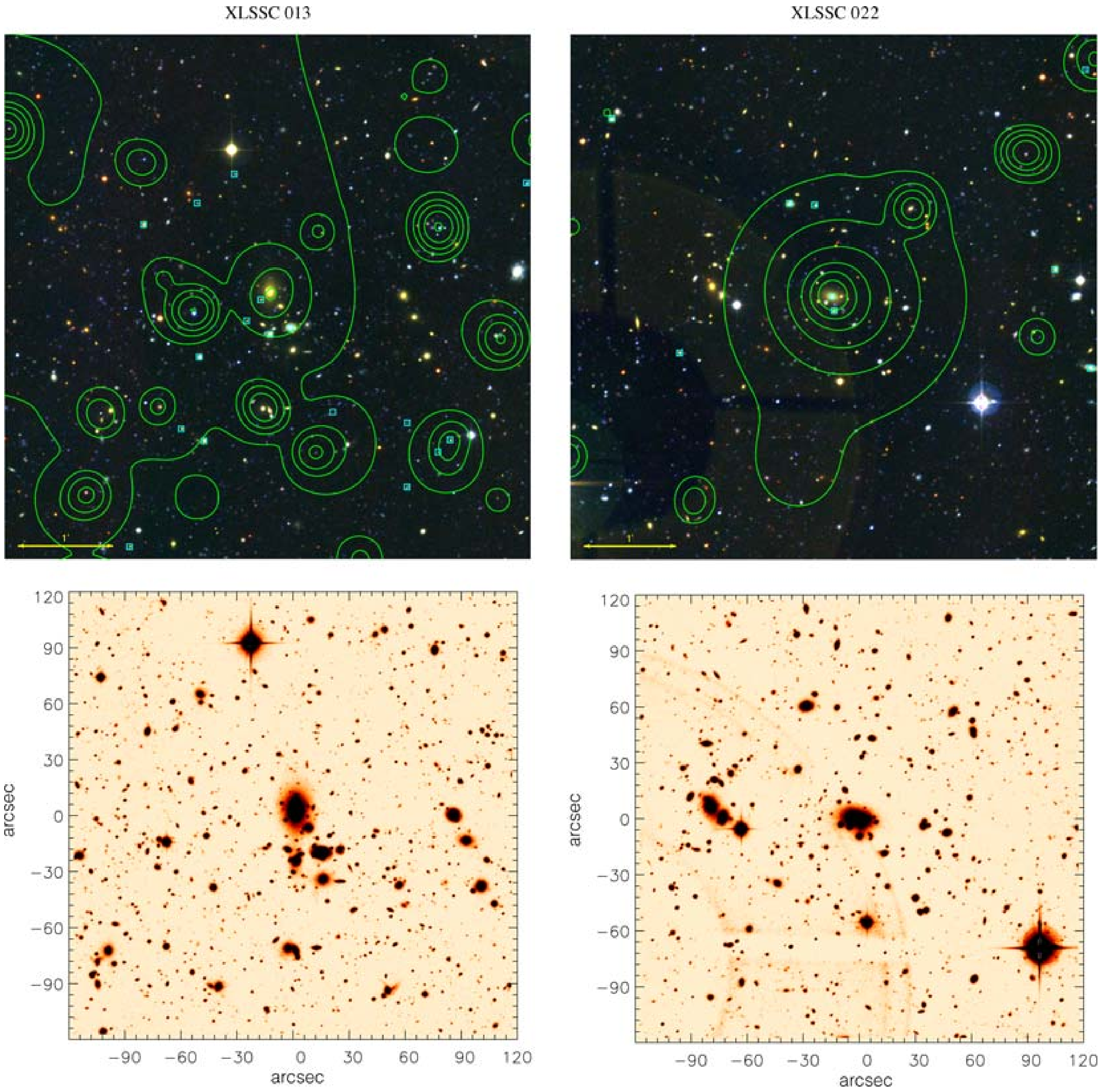
XLSSC 013

XLSSC 022

Figure B1 – *continued*

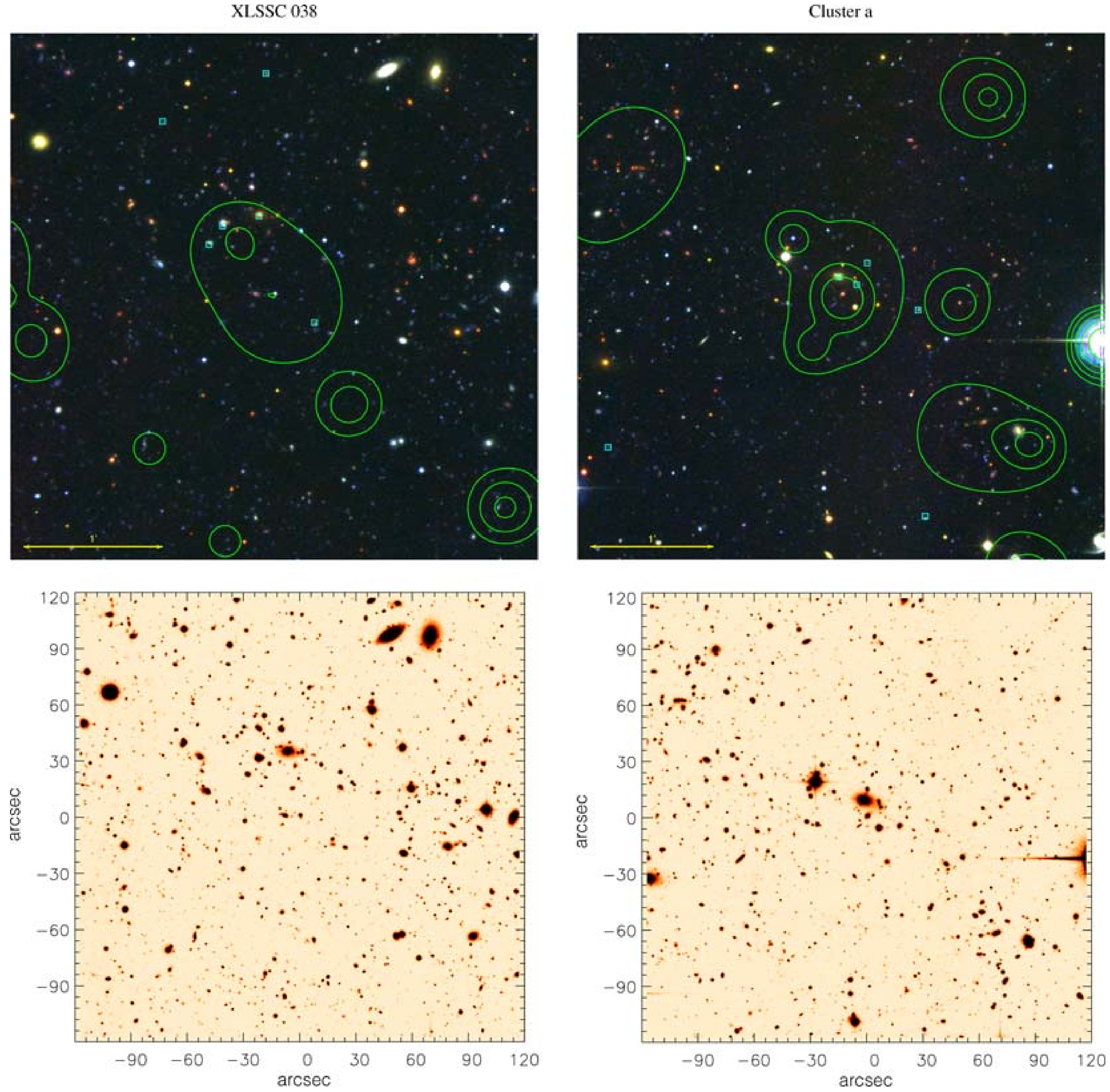

Figure B1 – *continued*

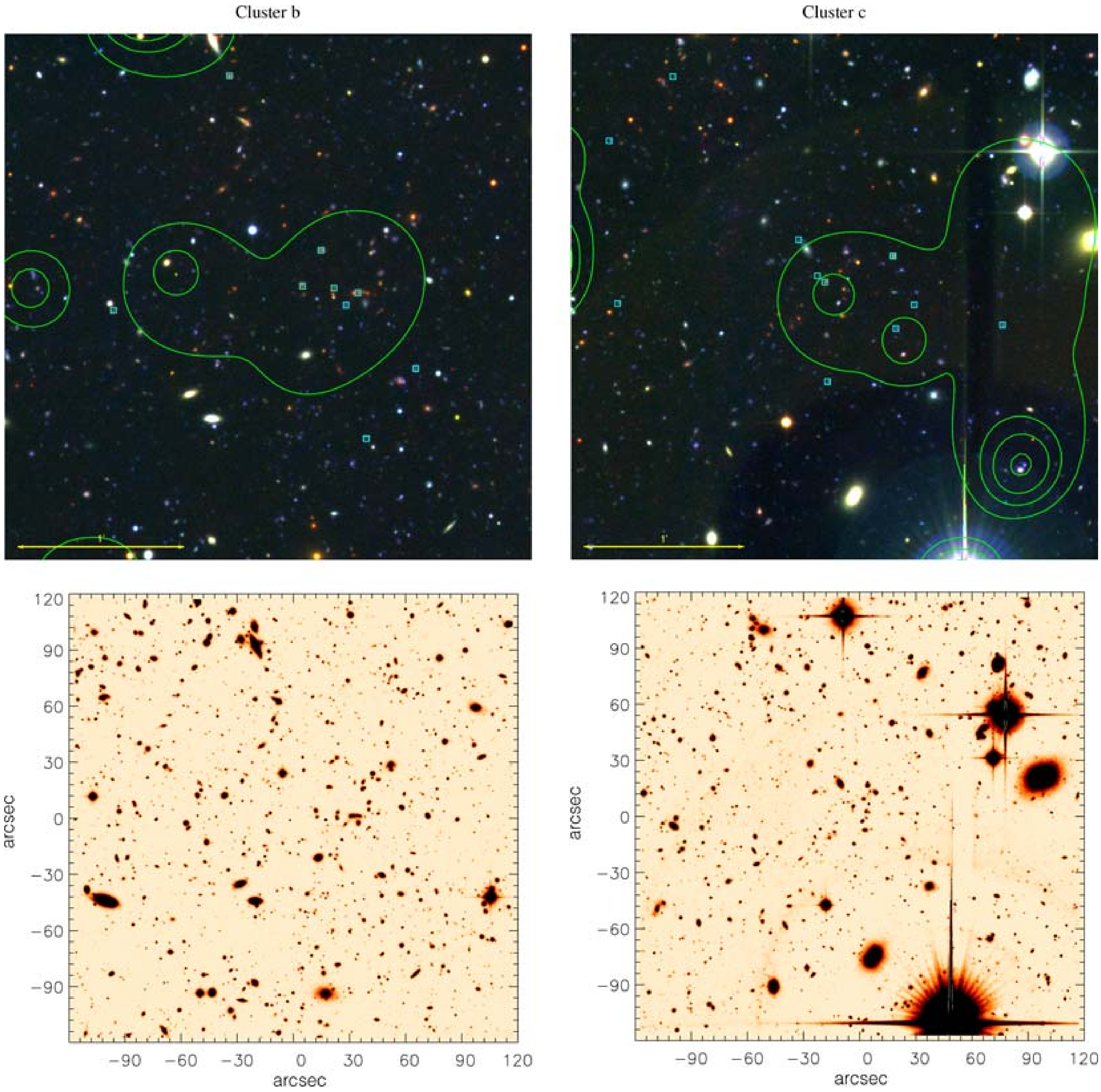

Figure B1 – *continued*

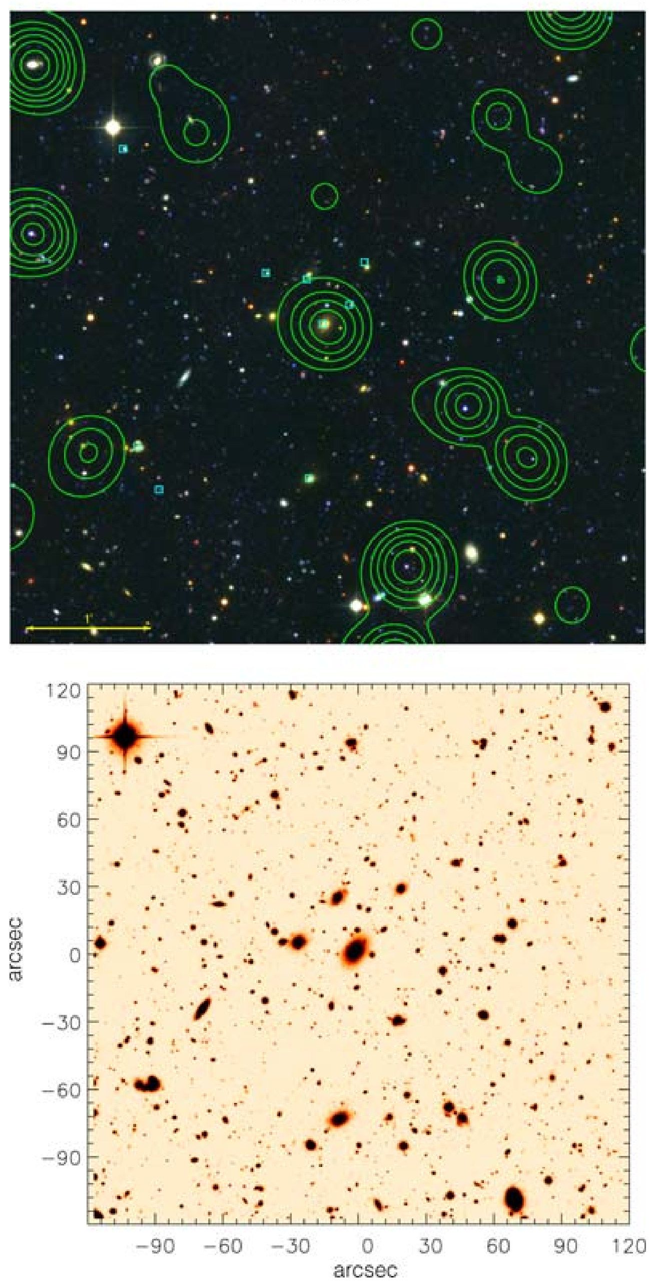

Cluster d

Figure B1 – *continued*

This paper has been typeset from a TEX/LATEX file prepared by the author.